Transient Synchronization Stability of Grid-Following Converters Considering Nonideal Current Loop

Chao Charles Liu, *Student Member, IEEE*, Jingxi Yang, *Member, IEEE*, Chi K. Tse, *Fellow, IEEE*, and Meng Huang, *Member, IEEE*

***Abstract*—The widely deployed grid-following converters (GFLCs) may lose synchronization under grid disturbances, presenting a critical challenge to the power electronics penetrated power grid. Existing methods for analyzing transient synchronization stability often assume an ideal current loop in order to keep the system model at low order. However, such approaches based on a simplified second-order model can lead to optimistic stability prediction and inappropriate design. This article applies a full-order model to explore the effects of the nonideal current loop. The unstable periodic orbits (UPOs) that determine the basin of attraction of the stable equilibrium point are located via a numerical continuation method. Moreover, the essential bifurcations leading to the emergence and disappearance of UPOs are identified. A design principle with consideration of the effects of the nonideal current loop is derived to enhance the transient synchronization stability of GFLCs. Experimental results are provided to verify the analytical findings.**

***Index Terms*—Basin of attraction (BOA), current loop, grid-following converter (GFLC), numerical continuation, transient synchronization stability.**

I. Introduction

THE increased penetration of power electronics converters is reshaping the dynamical characteristics of the power grid, which has been dominated by synchronous generators for decades [1]. While new concepts, such as grid-forming converters (GFMCs), have been proposed, grid-following converters (GFLCs) are widely adopted in applications due to the relatively mature control methods applicable to GFLCs [2]. As Fig. 1 shows, the GFLC synchronizes with the grid via a phase-locked loop (PLL). However, both industry and academia have identified multiple stability problems of this control scheme [3], [4], [5]. One example is the GFLC tripping after the transmission system faults in California, where the North American Electric Reliability Corporation (NERC) identified the cause being the loss of synchronization (LOS) of the PLL [3].

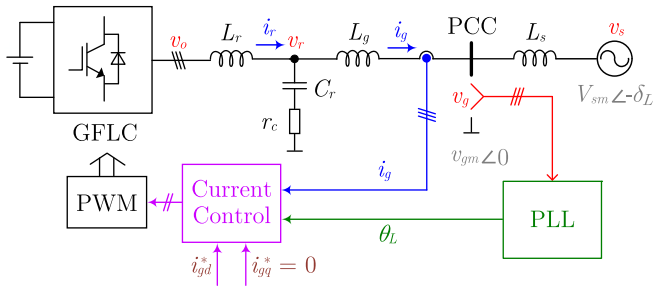

Fig. 1. Circuit diagram and control of the GFLC.

Depending on the assumed disturbance scale, the stability problems of the GFLC can be classified into small-signal stability and transient stability. Small-signal studies based on the small disturbance assumption simplify the analysis by linearizing the system, where the standard second-order system [6], the Bode plot [7], the impedance (admittance) methods [8], [9], and the damping analysis [10] can be applied. Some works considered the PLL and other control loops separately in the modeling process [6], [7], [10]. Under this paradigm, with each control loop being kept stable individually, the whole system can still become unstable due to the coupling between different control loops. This problem has been studied using the impedance methods [8], [9], which usually derive a sufficient condition for small-signal stability regarding the bandwidth of different control loops. Harnefors et al. [8] proposed to set the PLL bandwidth to less than one-tenth of the current loop bandwidth. On the other hand, Li et al. [9] determined the maximum PLL bandwidth by the ratio between the current loop bandwidth and the switching frequency. Despite their different conclusions, both studies have recommended a current loop much faster than the PLL.

The time-scale separation between the PLL and the current loop has also been introduced into the transient stability studies, which deal with large disturbances that make the linearized models inapplicable. The slow-scale dynamics of the PLL have been considered dominant in the transient synchronization stability.

Manuscript received 7 April 2023; revised 24 June 2023; accepted 4 August 2023. Date of publication 9 August 2023; date of current version 22 September 2023. This work was supported in part by the Hong Kong Research Grants Council under Grant GRF 112071/21 and in part by the City University of Hong Kong under Grants 9229105 and 9380114. Recommended for publication by Associate Editor A. Davoudi. *(Corresponding author: Jingxi Yang.)*

Chao Charles Liu, Jingxi Yang, and Chi K. Tse are with the Department of Electrical Engineering, City University of Hong Kong, Kowloon, Hong Kong (e-mail: chao.liu@my.cityu.edu.hk; jyang264@cityu.edu.hk; chitse@cityu.edu.hk).

Meng Huang is with the School of Electrical Engineering and Automation, Wuhan University, Wuhan 430072, China (e-mail: meng.huang@whu.edu.cn).

Color versions of one or more figures in this article are available at https://doi.org/10.1109/TPEL.2023.3303447.

Digital Object Identifier 10.1109/TPEL.2023.3303447

As a result, the PLL-based second-order model has been widely adopted in the literature [7], [11], [12], [13], [14], [15], [16]. Two primary mechanisms for the LOS under large disturbances have been revealed. The nonexistence of a stable equilibrium point (SEP) was found to result from reactive current support required by the grid code [7]. However, even when an SEP exists, LOS can still occur as the state trajectory leaves the SEP's basin of attraction (BOA) [5]. Typical grid disturbances, such as phase jumps, voltage dips, and short-circuit faults, can steer the state to the outside of the BOA.

The BOA analysis necessitates the use of large-signal methods. Considering the structural similarity between the second-order model of the GFLC and the swing equation of the synchronous generator, Hu et al. [11] introduced the equal-area criterion to estimate the BOA. This method is basically a special case of the energy function method [12], [13], which has the disadvantage of intrinsic conservation. On the other hand, Wu and Wang [14] applied the numerical phase portrait to evaluate the effects of parameters. Furthermore, Zhao et al. [15] derived an approximate analytical solution of the state trajectory via the averaging method, where the convergence or divergence of the trajectory could be judged by the relationship between parameters. To explain the qualitative change in the PLL dynamics, Ma et al. [16] identified some critical bifurcations of the second-order model, including a homoclinic bifurcation and a subcritical Hopf bifurcation. Nevertheless, one homoclinic bifurcation in the upper phase plane was missing in their work.

All these studies have assumed an ideal current loop, i.e., the output current perfectly follows the control reference. While this approach can approximately explain the behavior of GLFCs, neglecting the current transients inevitably leads to inaccurate transient stability assessment [17]. Moreover, according to Shil'nikov theorem, the essential bifurcation of GFLCs (i.e., homoclinic bifurcation) can be considerably complex if the system's dimension exceeds two [18]. Hence, the assumption of an ideal current loop could bury the essential qualitative changes.

Recently, the impact of the nonideal current loop has begun to be recognized. Chen et al. [17] showed a more accurate stability assessment by neglecting only the filter dynamics and keeping the current loop dynamics. In addition, Hu et al. [19] proposed an analogy between the current loop of GFLCs and the excitation control of synchronous generators. With delicate simplifications and empirical analysis, their study indicated that the current loop could increase the LOS risk by accelerating the PLL's equivalent motion after disturbances. Furthermore, Fu et al. [20] applied the extended invariance principle to identify the maximum dynamic interaction of the current loop in the sense of Lyapunov stability.

Existing works provide a qualitative description of the adverse effects of current transients on transient synchronization stability. However, the exact capability to maintain synchronization with different circuit and control parameters is yet to be clarified. Hence, the resulting analysis could not result in a quantitative design principle to enhance the stability of the GFLC. The challenge that prevents the consideration of the nonideal current loops lies in the difficulty of analyzing a high-order model, for which conventional methods adopted for second-order models become infeasible.

On the other hand, theoretical analysis has shown that the exact BOA is determined by the equilibrium points and periodic orbits on the BOA boundary [21]. Specifically, the union of the stable manifolds of these equilibrium points and periodic orbits forms the BOA boundary. In the second-order model, the unstable periodic orbit (UPO) emerging from a homoclinic bifurcation forms the BOA boundary [16]. Hence, an intuitive idea is to find the related periodic orbits in the full-order model using alternative methods.

To fill the gap, a numerical continuation method is introduced in this article. This method computes the curve of equilibrium points, periodic orbits, or bifurcations by solving the boundary value problems [18]. The existing studies tend to apply this method in the analysis of equilibrium points [22], [23]. In this article, we present a method that uses the full-order model to locate UPOs emerging from homoclinic bifurcations. To apply the numerical continuation method, we first estimate the initial points effectively using the second-order model. Our numerical continuation results reveal the complex bifurcation behavior captured by the full-order model. In this study, we have established a parameter design principle that ensures transient synchronization stability. Furthermore, we have systematically analyzed the effects of the current loop bandwidth and the voltage feedforward weight. These effects can be incorporated into our proposed design principle.

II. System Modeling

A. Limitation of Second-Order Model

As Fig. 1 shows, the GFLC connects the power grid via an *LCL* filter. The power grid is modeled as a voltage source v_s and a grid impedance, where the amplitude and frequency of v_s are V_{sm} and ω_0, respectively, and the grid impedance includes an inductance L_s and a resistance r_s. The PLL uses a proportional–integral controller to produce the phase reference of the current loop θ_L according to the voltage of the point of common coupling (PCC) v_g. In the dq-frame, the corresponding components of v_g are denoted by v_{gd} and v_{gq}. This representation is also adopted by other current and voltage variables unless stated otherwise. The dynamics of the PLL can be described by

$$\frac{\mathrm{d}y_\omega}{\mathrm{d}t} = v_{gq} \tag{1}$$

$$\frac{\mathrm{d}\delta_L}{\mathrm{d}t} = \omega_L - \omega_0 \tag{2}$$

$$\omega_L = \kappa_p v_{gq} + \kappa_i y_\omega + \omega_0 \tag{3}$$

where y_ω is the state variable of the PLL controller, δ_L is the phase difference between v_g and v_s, ω_L is the frequency of the PLL, and κ_p and κ_i are the proportional and integral parameters, respectively.

Using Park transformation, v_{gq} can be represented as

$$v_{gq} = -V_{sm}\sin\delta_L + i_{gd}\omega_L L_s + i_{gq} r_s. \tag{4}$$

As shown in Fig. 2, the difference between the full-order model and the second-order model lies in the modeling of i_{gd} and i_{gq}. Specifically, the full-order model considers the nonideal

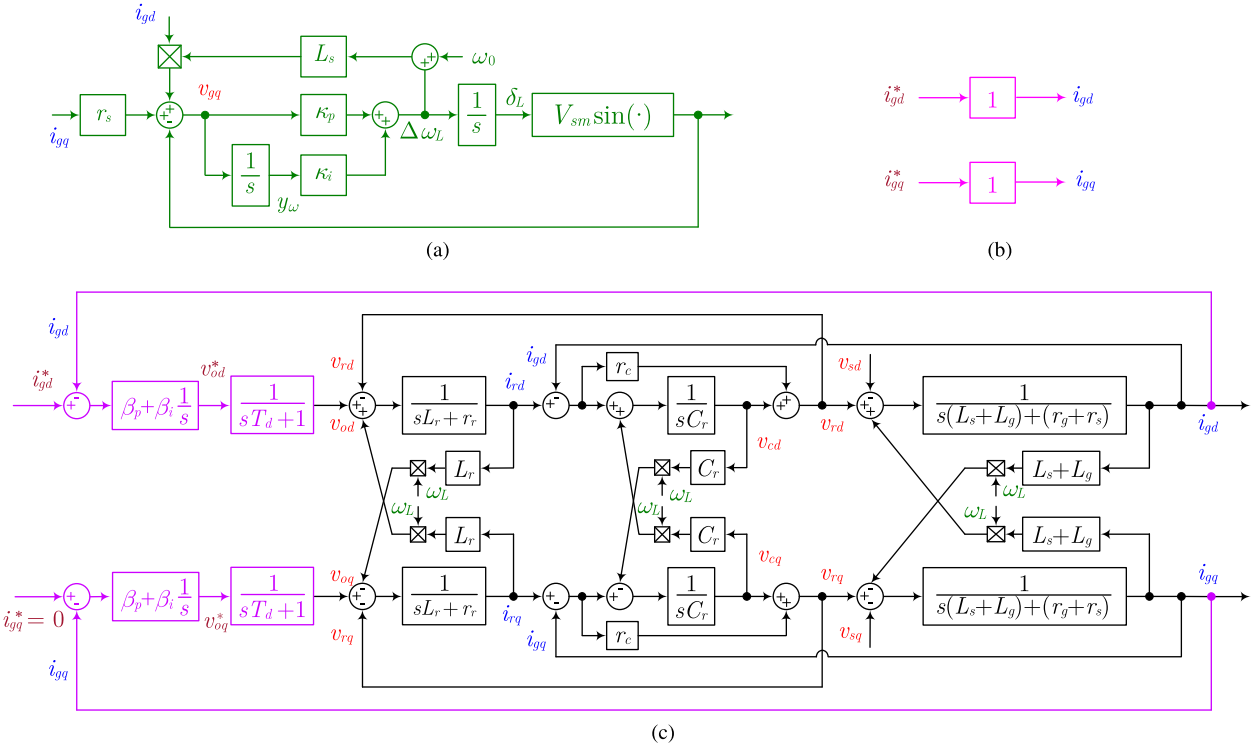

Fig. 2. Large-signal models of (a) PLL, (b) ideal current loop, and (c) nonideal current loop.

TABLE I
DEFAULT PARAMETERS OF GFLC

Parameter	Value	p.u.	Parameter	Value	p.u.
V_{sm}	311 V	1	L_r	2 mH	0.061
L_s	5 mH	0.152	r_r	0.1 Ω	0.010
r_s	0.1 Ω	0.010	C_r	60 μF	0.195
i^*_{gd}	30 A	1	r_c	1 Ω	0.096
i^*_{gq}	0	0	L_g	0.6 mH	0.018
κ_p	0.413	1	r_g	0.05 Ω	0.005
κ_i	7.786	1	ω_0	100π rad/s	1
β_p	1.648	1	$T_{\rm ctr}$	0.25 ms	0.125
β_i	51.779	1	$f_{\rm sw}$	2 kHz	40

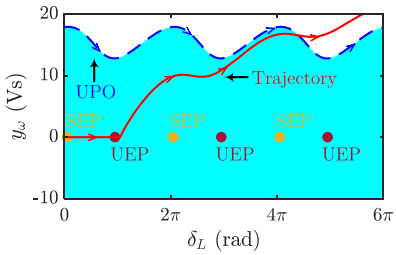

Fig. 3. SEP's BOA (the blue area) predicted by the second-order model and the state trajectory (the red curve) of the cycle-by-cycle simulation with $\kappa_p = 0.4$ p.u.

current loop in Fig. 2(c). On the other hand, the second-order model adopts the ideal current loop in Fig. 2(b), which assumes perfect current regulation, i.e.,

$$\begin{cases} i_{gd} = i^*_{gd} \\ i_{gq} = i^*_{gq} \end{cases} \tag{5}$$

where $i^*_{gq} = 0$ normally.

Equations (1)–(5) complete the second-order model [7], [11], [12], [13], [14], [15], [16]. The default parameters in Table I are designed using Bode plots to ensure small-signal stability, where the bandwidth of the PLL and current loop are $f_c^{\rm pll} = 23.36$ Hz and $f_c^{\rm cl} = 126.29$ Hz, respectively.

To see the limitation of the second-order model, a phase jump disturbance of $-\pi$ rad applied to v_s is presented in Fig. 3. The default parameters are adopted except that κ_p is set as 0.4 per unit (p.u.), with $f_c^{\rm pll}$ decreasing to 14.40 Hz. Since the current loop is much faster than the PLL, the precondition of the second-order model is satisfied. As predicted by the second-order model, two UPOs form the SEP's BOA boundary, within which all points should converge to the SEP. Clearly, the system's state lies in the BOA after the phase jump. However, the cycle-by-cycle simulation on MATLAB/Simulink shows that the state trajectory eventually diverges to infinity (limited by the overmodulation saturation in practice). This discrepancy indicates that neglecting the dynamics of the nonideal current loop leads to optimistic BOA prediction.

B. Full-Order Model

In view of the inaccuracy of the second-order model, a nonideal current loop, as shown in Fig. 2(b), is considered. The current loop generates the pulsewidth modulation (PWM) reference of the converter terminal voltage v_o^*, as follows:

$$\frac{\rm d}{{\rm d}t}\begin{bmatrix} y_{id} \\ y_{iq} \end{bmatrix} = \begin{bmatrix} i^*_{gd} \\ i^*_{gq} \end{bmatrix} - \begin{bmatrix} i_{gd} \\ i_{gq} \end{bmatrix} \tag{6}$$

$$\begin{bmatrix} v_{od}^* \\ v_{oq}^* \end{bmatrix} = \beta_p \left(\begin{bmatrix} i_{gd}^* \\ i_{gq}^* \end{bmatrix} - \begin{bmatrix} i_{gd} \\ i_{gq} \end{bmatrix} \right) + \beta_i \begin{bmatrix} y_{id} \\ y_{iq} \end{bmatrix} \tag{7}$$

where y_{id} and y_{iq} are the state variables of the current loop, and β_p and β_i are the proportional and integral parameters, respectively.

The converter terminal voltage v_o is affected by the time delay, which can be modeled as

$$\frac{\mathrm{d}}{\mathrm{d}t} \begin{bmatrix} v_{od} \\ v_{oq} \end{bmatrix} = \frac{1}{T_d} \left(\begin{bmatrix} v_{od}^* \\ v_{oq}^* \end{bmatrix} - \begin{bmatrix} v_{od} \\ v_{oq} \end{bmatrix} \right) \tag{8}$$

where $T_d = 1.5T_{\mathrm{ctr}}$ is the equivalent time constant, and T_{ctr} is the control period.

Finally, the grid-side current i_g is determined by the dynamics of the *LCL* filter and grid impedance. The *LCL* filter includes a converter-side inductance L_r, a capacitance C_r, a damping resistance r_c, and a grid-side inductance L_g, where the stray resistances of L_r and L_g are denoted by r_r and r_g, respectively. Thus, the dynamics of the filter and grid impedance are described by

$$\frac{\mathrm{d}}{\mathrm{d}t} \begin{bmatrix} i_{rd} \\ i_{rq} \end{bmatrix} = \frac{1}{L_r} \left(\begin{bmatrix} v_{od} \\ v_{oq} \end{bmatrix} - \begin{bmatrix} v_{rd} \\ v_{rq} \end{bmatrix} - \begin{bmatrix} r_r & -\omega_L L_r \\ \omega_L L_r & r_r \end{bmatrix} \begin{bmatrix} i_{rd} \\ i_{rq} \end{bmatrix} \right) \tag{9}$$

$$\frac{\mathrm{d}}{\mathrm{d}t} \begin{bmatrix} v_{cd} \\ v_{cq} \end{bmatrix} = \frac{1}{C_r} \left(\begin{bmatrix} i_{rd} \\ i_{rq} \end{bmatrix} - \begin{bmatrix} i_{gd} \\ i_{gq} \end{bmatrix} - \begin{bmatrix} 0 & -\omega_L C_r \\ \omega_L C_r & 0 \end{bmatrix} \begin{bmatrix} v_{cd} \\ v_{cq} \end{bmatrix} \right) \tag{10}$$

$$\begin{aligned} \frac{\mathrm{d}}{\mathrm{d}t} \begin{bmatrix} i_{gd} \\ i_{gq} \end{bmatrix} = \frac{1}{L_s + L_g} \Bigg(& \begin{bmatrix} v_{rd} \\ v_{rq} \end{bmatrix} - \begin{bmatrix} v_{sd} \\ v_{sq} \end{bmatrix} \\ & - \begin{bmatrix} r_s + r_g & -\omega_L (L_s + L_g) \\ \omega_L (L_s + L_g) & r_s + r_g \end{bmatrix} \begin{bmatrix} i_{gd} \\ i_{gq} \end{bmatrix} \Bigg) \end{aligned} \tag{11}$$

and

$$\begin{bmatrix} v_{rd} \\ v_{rq} \end{bmatrix} = \begin{bmatrix} v_{cd} \\ v_{cq} \end{bmatrix} + r_c \left(\begin{bmatrix} i_{rd} \\ i_{rq} \end{bmatrix} - \begin{bmatrix} i_{gd} \\ i_{gq} \end{bmatrix} \right) \tag{12}$$

where $v_{sd} = V_{sm} \cos \delta_L$, $v_{sq} = -V_{sm} \sin \delta_L$, i_{rd} and i_{rq} are the converter-side currents, v_{cd} and v_{cq} are the capacitance voltages, and v_{rd} and v_{rq} are the voltages across C_r and r_c.

Also, a more numerically stable representation of v_{gq} can be found as follows:

$$\begin{aligned} v_{gq} = \frac{L_s L_g}{L_s + L_g} \Bigg(& \frac{1}{L_s} v_{sq} + \frac{1}{L_g} v_{rq} \\ & + \left(\frac{r_s}{L_s} - \frac{r_g}{L_g} \right) i_{gq} \Bigg). \end{aligned} \tag{13}$$

Combining (1)–(3) and (6)–(13) yields a 12th-order nonlinear system, which can be represented as

$$\frac{\mathrm{d}\boldsymbol{x}}{\mathrm{d}t} = f(\boldsymbol{x}) \tag{14}$$

where

$$\boldsymbol{x} = \begin{bmatrix} y_\omega & \delta_L & i_{rd} & i_{rq} & v_{cd} & v_{cq} & i_{gd} & i_{gq} & y_{id} & y_{iq} & v_{od} & v_{oq} \end{bmatrix}^{\mathrm{T}}$$

is the state vector.

III. Numerical Continuation for Bifurcation Analysis

A. Homoclinic Bifurcation

The homoclinic bifurcation occurs when a homoclinic orbit connects a saddle [18]. The saddle is an unstable equilibrium point (UEP) with both positive and negative eigenvalues. As a parameter changes, the split of the homoclinic orbit can generate a stable periodic orbit (SPO) or UPO, depending on the polarity of the saddle quantity. For a second-order system, the saddle quantity refers to the algebraic sum of the saddle's two eigenvalues.

This feature of the homoclinic bifurcation results in a dual characteristic between the GFMC and the GFLC. Our previous work has clarified that the homoclinic bifurcation generating an SPO is the cause of sustained low-frequency oscillation of the GFMC [24]. Then, a study based on the second-order model identified that the homoclinic bifurcation generating a UPO leads to the qualitative changes of transient synchronization stability of the GFLC [16]. It is reasonable to expect this bifurcation to remain in the full-order model since the slow dynamics of the PLL are dominating for the GFLC.

However, the homoclinic bifurcation can have distinctive features in high-order systems. From the homoclinic central manifold theorem [18], the leading eigenvalues, instead of all eigenvalues, determine the property of the homoclinic bifurcation. The leading eigenvalues are defined as the eigenvalues that are closest to the imaginary axis. For a saddle with eigenvalues satisfying

$$\mathrm{Re}(\lambda_a) < \ldots < \mathrm{Re}(\lambda_1) < 0 < \mathrm{Re}(\lambda_2) < \ldots < \mathrm{Re}(\lambda_b)$$

the leading stable and unstable eigenvalues are λ_1 and λ_2, respectively. Then, the saddle quantity is given as

$$\sigma = \mathrm{Re}(\lambda_1) + \mathrm{Re}(\lambda_2). \tag{15}$$

As in the case of the second-order system, $\sigma < 0$ in high-order systems means an SPO emerging from bifurcation. In contrast, Shil'nikov theorem [18] predicts that $\sigma > 0$ in high-order systems can have following two different results.

1) *One simple UPO:* This case occurs when the leading eigenvalues are both real values, i.e., $\mathrm{Im}(\lambda_1) = \mathrm{Im}(\lambda_2) = 0$. This saddle is referred to as the Type-1 saddle in the following.
2) *Infinite UPOs and one chaotic attractor:* This case occurs when at least a pair of leading eigenvalues are complex, i.e., $\mathrm{Im}(\lambda_1) \neq 0$ or $\mathrm{Im}(\lambda_2) \neq 0$. This saddle is referred to as the Type-2 saddle in the sequel.

B. Numerical Continuation

The adoption of the full-order model presents a crucial challenge. The analysis method for the second-order model is no longer applicable. For the second-order model, the stable and

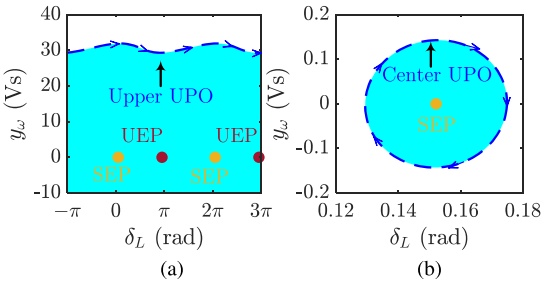

Fig. 4. UPOs emerging from the homoclinic bifurcations in the second-order model, where (a) $\kappa_p = 1$ p.u., and (b) $\kappa_p = 0.0092$ p.u.

unstable manifolds of the saddle can be calculated by integrating the model along the saddle's eigenvectors. A homoclinic orbit is found when the two manifolds overlap. However, the full-order model as a high-order system can be much stiffer in the inverse direction of time. Therefore, the calculation of the stable manifold easily fails as the integration errors blow up instantaneously [18].

In this article, we try to find the UPO emerging from the homoclinic bifurcation. To this end, the numerical continuation of UPOs is applied in a periodic boundary-value problem. Let the parametric representation of (14) be $f(\boldsymbol{x}, \alpha)$, where α is the selected continuation parameter. The time $t \in [0, T]$ can be normalized to $\tau \in [0, 1]$, where T is the period of the UPO $\boldsymbol{x}_t$. The normalized system can be represented as

$$\frac{\mathrm{d}\boldsymbol{\mu}}{\mathrm{d}\tau} = Tf(\boldsymbol{\mu}, \alpha) \tag{16}$$

where $\boldsymbol{\mu}_\tau$ is equivalent to $\boldsymbol{x}_t$. Hence, $\boldsymbol{\mu}_\tau$ is a UPO with period 1, and the periodic boundary condition is given as

$$\boldsymbol{\mu}_0 = \boldsymbol{\mu}_1. \tag{17}$$

The discretization of (16) and (17) defines a curve consisting of UPOs, i.e.,

$$\mathcal{F}(\boldsymbol{\xi}, \alpha) = 0,\ \mathcal{F} : \mathbb{R}^{N+1} \to \mathbb{R}^N. \tag{18}$$

With an additional phase condition, the periodic boundary-value problem defined by (18) can be solved via Newton-like iterations. Some well-studied test functions can be used to locate the bifurcation points along this curve. For implementation details, refer to Kuznetsov [18].

As the numerical continuation relies on iterations, the initial point to start the continuation is of great significance. By studying the second-order model, the rough features of the UPOs generated from the homoclinic bifurcations are already known. For the upper homoclinic bifurcation, the associated UPO behaves close to a straight line at relatively large κ_p, as shown in Fig. 4(a). For the center homoclinic bifurcation, the associated UPO converges to the SEP at relatively small κ_p, eventually leading to a subcritical Hopf bifurcation, as shown in Fig. 4(b). These features of the UPOs in the second-order model provide an effective estimation for the initial points. Therefore, for the full-order model, the continuation of the upper and center UPOs here starts from an approximate straight line and the subcritical Hopf bifurcation, respectively. The corresponding homoclinic orbits can be found when the periods of these UPOs approach infinity.

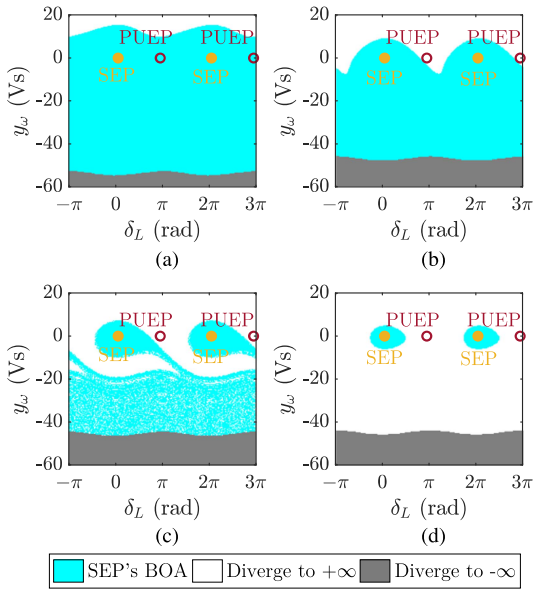

Fig. 5. BOA cross sections containing the SEP where (a) $\kappa_p = 1$ p.u., (b) $\kappa_p = 0.4$ p.u., (c) $\kappa_p = 0.26$ p.u., and (d) $\kappa_p = 0.22$ p.u. Other parameters adopt the default values. Note that the PUEP instead of the UEP is on these cross sections.

IV. Transient Synchronization Stability

A. Basin of Attraction

The full-order model is applied to derive the SEP's BOA numerically. Specifically, the trajectory starting from each initial state in the phase plane is calculated by the Runge–Kutta method. Convergence or divergence of the numerical process can be used to identify the BOA. As the system normally operates at the SEP, the BOA cross section containing the SEP is analyzed. Fig. 5 shows that the BOA cross section is connected at $\kappa_p = 1$ p.u., implying two potential UPOs in the upper and bottom sides. As κ_p decreases to 0.26 p.u., the BOA cross section splits into a fractal structure. Furthermore, the BOA cross section shrinks to an ellipse at $\kappa_p = 0.22$, suggesting a potential UPO near the SEP. If κ_p decreases further, the SEP eventually becomes a UEP via the subcritical Hopf bifurcation. These rough features are consistent with that of the second-order model, indicating the primary role of the PLL in the dynamics of the GFLC.

However, the comparison between Figs. 3 and 5(b) indicate that the BOA shrinks much faster in the full-order model. Consequently, the projection of the UEP (PUEP) in Fig. 5(b) becomes out of the BOA at relatively large κ_p. This significant difference can be attributed to the adverse effects of current transients. The result demonstrates that the second-order model overestimates the GLFC's robustness to phase jump disturbances, highlighting the importance of the nonideal current loop in the transient synchronization stability.

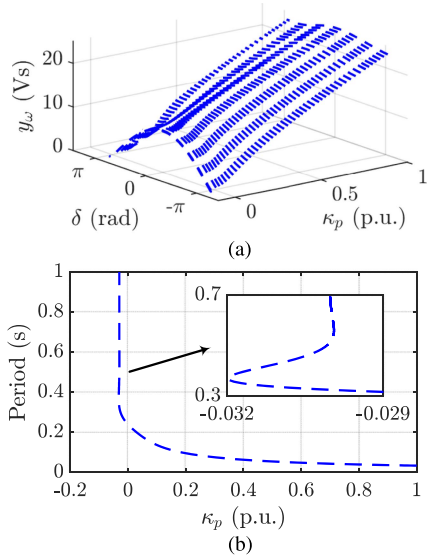

Fig. 6. (a) Projection of the upper UPO manifold, and (b) periods of the upper UPOs.

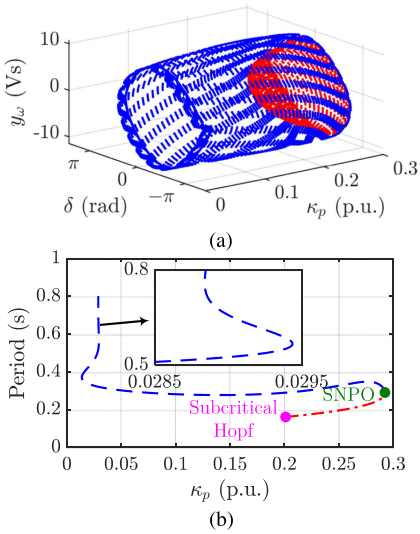

Fig. 7. (a) Projection of the center UPO manifold, and (b) periods of the center UPOs. Dashed and dash-dotted lines represent external and internal branches, respectively.

B. Bifurcation Behavior

The numerical continuation method is utilized to identify the bifurcation behavior behind the BOA changes. The continuation results of the upper and center UPOs are shown in Figs. 6 and 7, respectively. The manifolds in Figs. 6(a) and 7(a) show the trajectory variations of the corresponding UPOs with different κ_p. The periods of the UPOs in Figs. 6(b) and 7(b) approach infinity near $\kappa_p = 0$, implying homoclinic bifurcation. The saddle quantities at the upper and center homoclinic bifurcations are 24.52 and 27.44, respectively, with both the saddles having complex leading eigenvalues. Hence, as Shil'nikov theorem predicts, infinite UPOs will emerge near the homoclinic bifurcations. This phenomenon is verified by the repetitive small "wiggles" near the homoclinic bifurcations illustrated in Figs. 6(b) and 7(b).

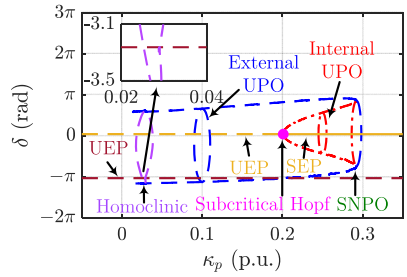

Fig. 8. Codim-1 bifurcation diagram regarding the center UPOs, where solid line represents the SEP, and dashed and dashed-dotted lines represent the UEPs and UPOs. All parameters except κ_p adopt the default values.

Fig. 6 shows that, within the normal parameter range (i.e., $\kappa_p > 0$), there exists at least an upper UPO whose stable manifold can affect the SEP's BOA. From (14), for any values of κ_p, the SEP lies in the same position, as shown in Fig. 5. Thus, Fig. 6 indicates that as κ_p decreases from 1 p.u., the upper UPO gets closer to the UEP and, simultaneously, the SEP, resulting in the BOA's contraction.

Moreover, Fig. 7 shows two main branches of UPOs in the center UPO manifold. For clarity, a codim-1 bifurcation diagram illustrating the center UPOs is presented in Fig. 8. The bifurcation diagram shows that the external and internal branches of the center UPOs emerge from the homoclinic and Hopf bifurcations, respectively. The internal branch makes the BOA significantly sensitive to parameter choices. As the internal branch approaches the SEP, the BOA cross section shrinks rapidly from a connected area ($\kappa_p = 0.292$ p.u.) to zero ($\kappa_p = 0.201$ p.u.) until a subcritical Hopf bifurcation sets in. To enhance the transient synchronization stability of the GLFC, the internal branch's existence should be avoided. This objective can be achieved by triggering the saddle-node bifurcation of periodic orbits (SNPO) at $\kappa_p = 0.292$ p.u., where the two branches collide and annihilate.

The significance of the SNPO is further illustrated in Fig. 9(a), where the magnitudes of the critical phase jumps $\Delta\theta_s$ leading to instability are presented. As κ_p decreases from the SNPO, the critical phase jumps drop to zero in a narrow parameter range. Therefore, the full-order model suggests triggering the SNPO to enhance the synchronization stability. In contrast, the critical phase jumps of the second-order model in Fig. 9(b) suggest triggering the upper homoclinic bifurcation at $\kappa_p = 0.166$ p.u. With this design principle derived from the second-order model, the real critical phase jumps have decreased to zero, indicating no BOA, as shown in Fig. 9(a). Therefore, comparing Fig. 9(a) and (b) validates the full-order model and the proposed design principle.

C. Effects of Current Loop Bandwidth

Studies have shown that a faster current loop can reduce the current transient and mitigate its adverse impact on the transient synchronization stability [17], [19]. In this section, not only the qualitative effects of the current loop bandwidth f_c^{cl}, but also its quantitative effects are studied in terms of the BOA and bifurcation behavior. With $f_c^{\mathrm{cl}} \leq 0.2 f_{\mathrm{sw}}$ [8], where $f_{\mathrm{sw}} = 2$ kHz is the

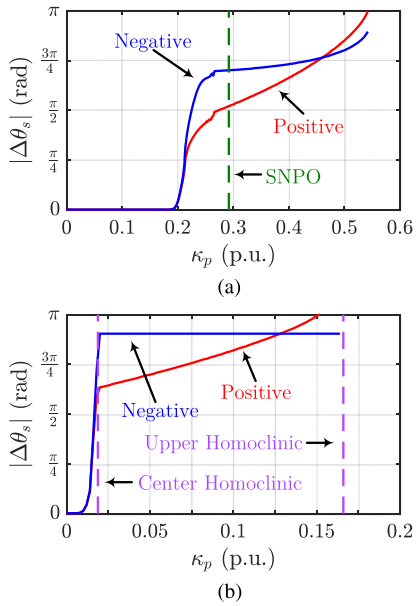

Fig. 9. Magnitudes of the critical phase jumps of (a) full-order model and (b) second-order model.

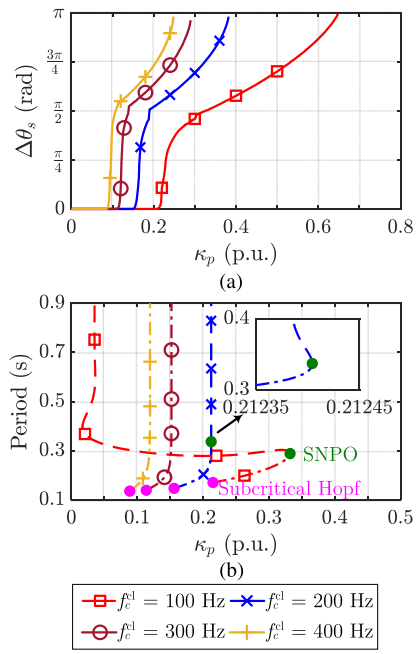

Fig. 10. (a) Positive critical phase jumps with different f_c^{cl}, and (b) periods of center UPOs with different f_c^{cl}, where dashed and dash-dotted lines represent external and internal branches, respectively.

switching frequency, four cases with $f_c^{cl} = 100$, 200, 300, and 400 Hz are presented in Fig. 10. The current loop bandwidth is tuned while the ratio β_i/β_p remains unchanged. Fig. 10(a) shows that increasing f_c^{cl} enlarges the BOA considerably. However, even with a very high bandwidth of 400 Hz, the discrepancy between the second-order model and full-order model is still significant, as shown in Figs. 9(b) and 10(a). Therefore, while the second-order model provides an approximate description of

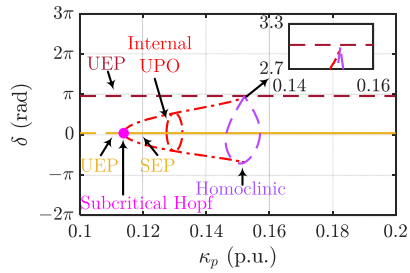

Fig. 11. Codim-1 bifurcation diagram illustrating the center UPO with $f_c^{cl} = 300$ Hz, where solid line represents the SEP, and dashed and dashed-dotted lines represent the UEPs and UPO. Other parameters adopt the default values.

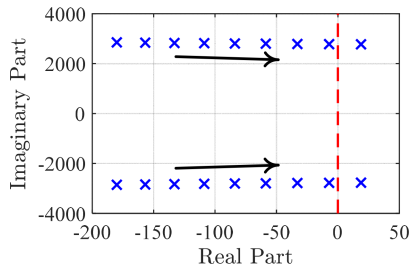

Fig. 12. Root loci of eigenvalues with f_c^{cl} varying from 900 to 1000 Hz.

the dynamical behavior, the current transient is important for accurate BOA estimation.

The changes in bifurcation behavior regarding the center UPOs are illustrated by Fig. 10(b). With $f_c^{cl} = 100$ Hz, the external branch of the center UPOs emerges from a homoclinic bifurcation at small κ_p (nearly zero). As f_c^{cl} increases to 200 Hz, another homoclinic bifurcation occurs at relatively large κ_p (over 0.2 p.u.), of which the generated UPO forms the external branch. If f_c^{cl} increases further, the SNPO and the external branch disappear. This phenomenon can be explained by applying Shil'nikov theorem. When $f_c^{cl} = 200$ Hz, the saddle's leading eigenvalues are $-21.52 \pm j16.78$ and 57.07, indicating a Type-2 saddle. When $f_c^{cl} = 300$ Hz, the leading eigenvalues change to -26.02 and 55.63, indicating a Type-1 saddle. Hence, the transformation of the saddle means that the homoclinic bifurcation generates only a simple UPO for very high f_c^{cl}. A codim-1 bifurcation diagram with $f_c^{cl} = 300$ Hz is presented in Fig. 11, where the only center UPO is directly connected by the subcritical Hopf bifurcation and the homoclinic bifurcation. Indeed, such bifurcation behavior of the full-order model at very high f_c^{cl} is similar to that of the second-order model, which can be regarded as a full-order model with infinite current loop bandwidth.

Nevertheless, the available bandwidth of the current loop is limited by small-signal stability as well as the switching frequency. As shown in the root loci plotted in Fig. 12, if the current loop bandwidth reaches 1000 Hz, the SEP will become unstable through the Hopf bifurcation. Thus, the extreme bandwidth of the current loop here is nearly 900 Hz in terms of small-signal stability. With such an extreme setting, the critical phase jumps of the full-order model are presented in Fig. 13, which is close to,

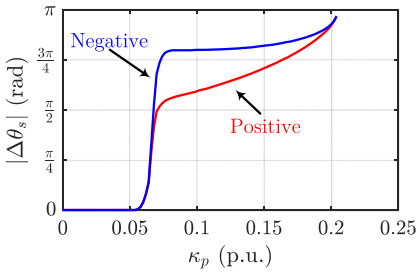

Fig. 13. Magnitudes of the critical phase jumps with $f_c^{\mathrm{cl}} = 900$ Hz.

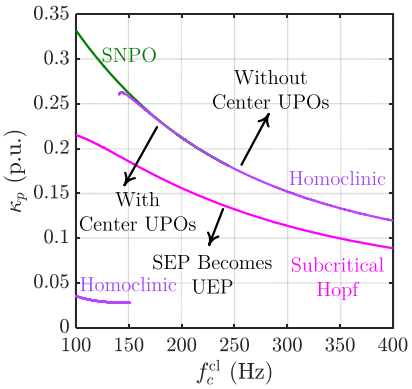

Fig. 14. Codim-2 bifurcation diagram in the $(f_c^{\mathrm{cl}}, \kappa_p)$-plane.

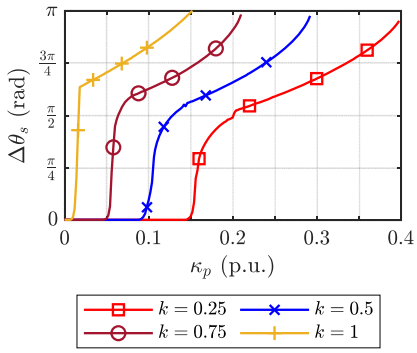

Fig. 15. Positive critical phase jumps with the voltage feedforward scheme.

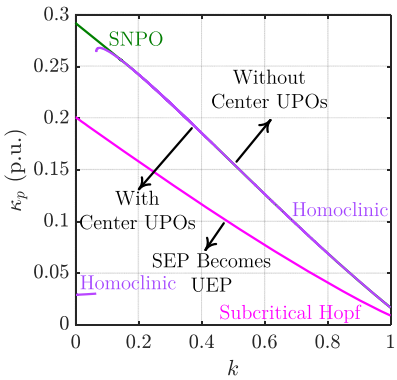

Fig. 16. Codim-2 bifurcation diagram in the (k, κ_p)-plane.

although not exactly same as, Fig. 9(b). Therefore, the second-order model cannot fully substitute the full-order model with only the current loop bandwidth being tuned. Besides, tuning the current loop bandwidth to adapt to the second-order model may cause other problems, e.g., reducing the small-signal stability margin. Thus, the appropriate model should be chosen according to the specific setting.

To clarify the bifurcation behavior with varying current loop bandwidth, a codim-2 bifurcation diagram is presented in Fig. 14. It can be observed that, at relatively low f_c^{cl}, the SNPO serves as the boundary between the existence and disappearance of the center UPOs. With f_c^{cl} exceeding 140.85 Hz, a center homoclinic bifurcation occurs near the SNPO and eventually overlaps with the SNPO at $f_c^{\mathrm{cl}} = 244.52$ Hz. Simultaneously, the saddle connected by the homoclinic orbit transforms from a Type-2 saddle to a Type-1 saddle. To enhance the transient synchronization stability, the existence of the center UPOs should be avoided. This objective can be achieved by triggering the SNPO for relatively low current loop bandwidth or avoiding the center homoclinic bifurcation for very high current loop bandwidth.

D. Effects of Voltage Feedforward Scheme

Although the PCC voltage is neglected in the derivation of the current loop bandwidth, it can significantly impact current regulation [25]. To address the current harmonics that result from voltage distortion, grid voltage can be feedforwarded into the current loop. This scheme is also crucial for transient stability, as it enhances the speed of the current loop. Thus, the output of the current controller in (7) can change to

$$\begin{bmatrix} v_{od}^* \\ v_{oq}^* \end{bmatrix} = \beta_p \left(\begin{bmatrix} i_{gd}^* \\ i_{gq}^* \end{bmatrix} - \begin{bmatrix} i_{gd} \\ i_{gq} \end{bmatrix} \right) + \beta_i \begin{bmatrix} y_{id} \\ y_{iq} \end{bmatrix} + k \begin{bmatrix} v_{gd} \\ v_{gq} \end{bmatrix} \tag{19}$$

where

$$v_{gd} = \frac{L_s L_g}{L_s + L_g} \left(\frac{1}{L_s} v_{sd} + \frac{1}{L_g} v_{rd} + \left(\frac{r_s}{L_s} - \frac{r_g}{L_g} \right) i_{gd} \right). \tag{20}$$

Here, a feedforward weight $k \in [0, 1]$ is adopted because the unweighted voltage feedforward scheme will increase the risk of small-signal instability of converters with *LCL* filters, especially under weak grids [26].

Fig. 15 shows the positive critical phase jumps of the full-order model adopting the voltage feedforward scheme. As k varies from 0 to 1, the BOA of the full-order model gradually becomes close to that of the second-order model. Furthermore, the bifurcation behavior with varying k is illustrated by the codim-2 bifurcation diagram in Fig. 16. Similar to increasing f_c^{cl}, increasing k leads to the change of the bifurcation behavior from Figs. 8 to 11. The reason is that both increasing f_c^{cl} and k can accelerate current regulation.

Furthermore, the full-order model gives the same BOA and bifurcation behavior as the second-order model for an extreme k (i.e., 1), but not for an extreme f_c^{cl} (i.e., 800 Hz). Thus, the

TABLE II
QUALITATIVE EFFECTS OF PARAMETERS

PLL	κ_p ↑	κ_i ↓	
Current Loop	i_{gd}^* ↓	f_c^{cl} ↑	k ↑
Grid	V_{sm} ↑	L_s, r_s ↓	

Note: "↑" ("↓") denotes that the transient synchronization stability can be enhanced by increasing (decreasing) the corresponding parameter.

simplification of the second-order model is valid for the GFLCs using the unweighted voltage forward scheme, although this scheme can lead to oscillations under a high grid impedance [26]. Besides, regardless of the choice of f_c^{cl} and k, the full-order model and the numerical continuation are always valid.

V. IMPLICATIONS FOR DESIGN

A. Design-Oriented Analysis

As a classical application of bifurcation diagrams, design-oriented analysis can be conveniently performed with the full-order model. The bifurcation diagrams corresponding to the SNPO and the center homoclinic bifurcation with different control and grid parameters are provided in Fig. 17. As summarized in Table II, the qualitative effects of the parameters on the BOA, except f_c^{cl} and k, in the full-order model are the same as in the second-order model [15].

However, the desired parameters vary significantly with the current loop bandwidth. For instance, when f_c^{cl} decreases from 300 to 150 Hz with other parameters remaining unchanged, the minimum required κ_p gets nearly doubled (from 0.152 to 0.262 p.u.). Suppose κ_p above the bifurcation boundary by 0.05 p.u. is adopted. Then, system A ($\kappa_p = 0.202$ p.u.) in Fig. 17(a) should be chosen for $f_c^{\mathrm{cl}} = 300$ Hz. On the other hand, the conventional methods neglecting the current transients recommend the same κ_p for different current loop bandwidth, which may lead to system B ($\kappa_p = 0.202$ p.u., $f_c^{\mathrm{cl}} = 150$ Hz) in Fig. 17(a). For such lower f_c^{cl}, the proposed method suggests choosing system C ($\kappa_p = 0.312$ p.u.) in Fig. 17(a) to ensure transient synchronization stability.

The BOA cross sections of systems A–C are provided in Fig. 18. Clearly, the BOA of systems A and C is significantly larger than that of system B. The robust performance of systems A and C can be further reflected by the critical clearing time t_c against voltage dips and short-circuit faults. The voltage dip is modeled as the temporary drop of the amplitude of the grid voltage to V_{sm}^f. Likewise, the short-circuit fault is modeled as the temporary increase of the inductance and resistance of the grid impedance to L_s^f and r_s^f, respectively. After the fault is cleared, the grid voltage and impedance are assumed to recover to the default values. The critical clearing time to remain stable is presented in Fig. 19. For a voltage dip with $V_{sm}^f = 0.35$ p.u., systems A, B, and C must clear the fault within 0.30 s, 0.05 s, and 0.09 s, respectively. Such difference is also significant for a short-circuit fault with $L_s^f = 1.8$ p.u. and $r_s^f = 1.8$ p.u., where t_c of systems A–C are 1.01 s, 0.47 s, and 0.88 s, respectively. The results show

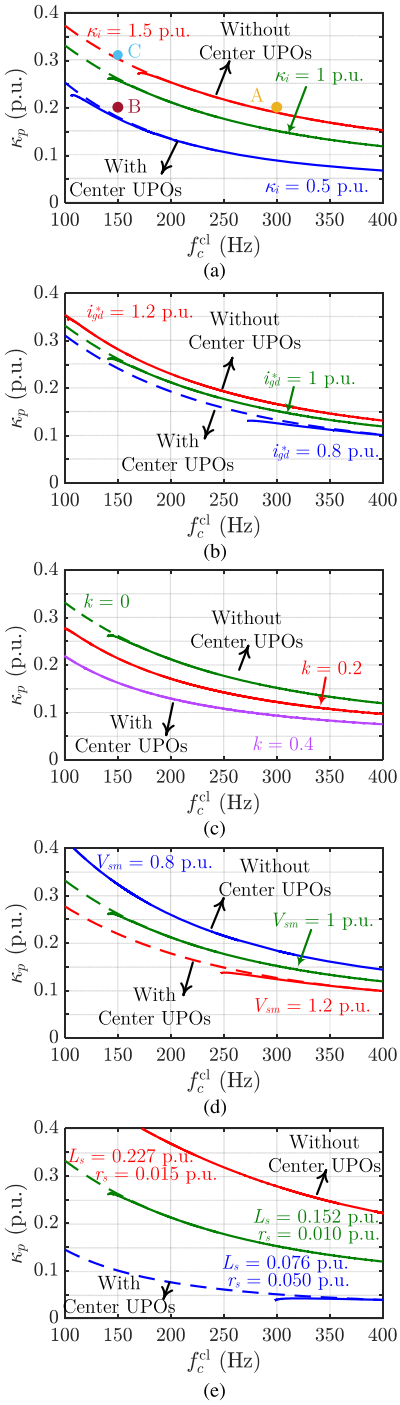

Fig. 17. Bifurcation diagrams in the $(f_c^{\mathrm{cl}}, \kappa_p)$-plane with varying (a) κ_i, (b) i_{gd}^*, (c) k, (d) V_{sm}, and (e) L_s and r_s. Dashed and solid lines represent the SNPO and homoclinic bifurcations, respectively.

that systems A and C have more time to clear the relatively severe faults. In contrast, system B, designed without considering the current transients, is more likely to become unstable with a short duration of grid faults. Hence, the bifurcation analysis with the full-order model enables a more accurate design reflecting the adverse effects of the nonideal current loop, and is applicable to different current loop parameters.

TABLE III
TWO DESIGN PRINCIPLES

Design boundary	Model	Analysis method	Applicability	Limitation
Upper homoclinic bifurcation	Second-order	Direct integration	With unweighted voltage feedforward scheme	Small-signal stability margin
SNPO or center Homoclinic bifurcation	Full-order	Numerical continuation	Whole parameter range	Complex computation

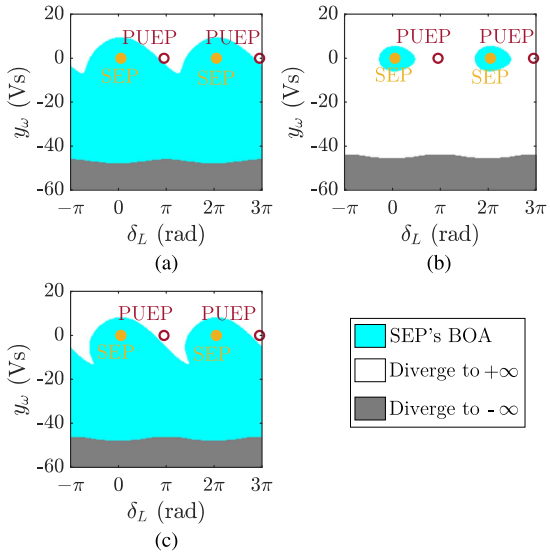

Fig. 18. BOA cross sections containing the SEP where (a) $\kappa_p = 0.202$ p.u., $f_c^{\rm cl} = 300$ Hz, (b) $\kappa_p = 0.202$ p.u., $f_c^{\rm cl} = 150$ Hz, (c) $\kappa_p = 0.312$ p.u., and $f_c^{\rm cl} = 150$ Hz. Other parameters adopt the default values.

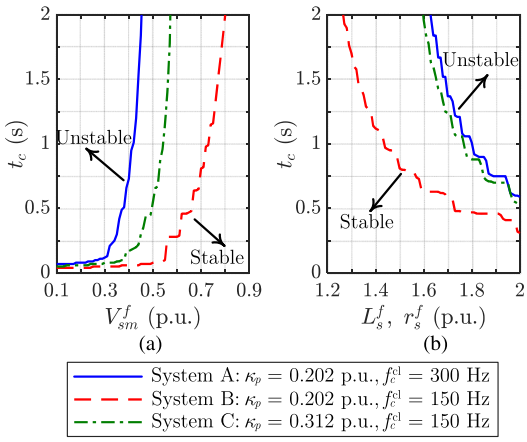

Fig. 19. Critical clearing time for (a) voltage dips and (b) short-circuit faults.

B. Discussion on Applications of Design Principles

Two design principles can be applied in various applications based on the second-order and full-order models. Their applicability and limitations have been summarized in Table III. The second-order model's design boundary can be identified through direct integration, but its accuracy is only suitable for GFLCs that use the unweighted voltage feedforward scheme. Using this method comes at the expense of less small-signal stability margin. On the other hand, the full-order model's design principle has a broad range of applicability. For engineers and researchers without a strong background in numerical bifurcation analysis, identifying the design boundary through numerical continuation can be complex. Fortunately, open-source tools, such as MATCONT [27], have simplified the computation process.

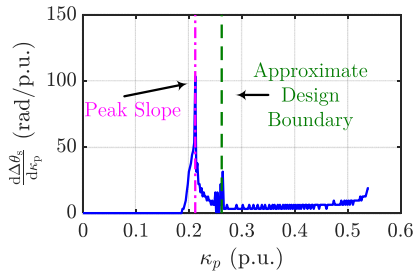

Fig. 20. Slope of the positive critical phase jumps with respect to κ_p. Other parameters adopt the default values.

TABLE IV
COMPARISON OF DESIGN BOUNDARIES

Case	Exact κ_p	Approximate κ_p	Error
$f_c^{\rm cl} = 100$ Hz	0.332 p.u.	0.268 p.u.	-0.064 p.u.
$f_c^{\rm cl} = 126.29$ Hz	0.292 p.u.	0.262 p.u.	-0.030 p.u.
$f_c^{\rm cl} = 200$ Hz	0.212 p.u.	0.214 p.u.	0.002 p.u.
$f_c^{\rm cl} = 300$ Hz	0.152 p.u.	0.170 p.u.	0.018 p.u.
$f_c^{\rm cl} = 400$ Hz	0.120 p.u.	0.146 p.u.	0.026 p.u.
Mean	-	-	-0.006 p.u.

An alternative method is proposed to identify the approximate design boundary in addition to proper numerical continuation, which facilitates practical applications. The exact design boundary (e.g., SNPO) is crucial because a UPO emerges at this boundary, making the BOA highly sensitive to parameter changes. Therefore, the approximate design boundary can be found near the peak of the BOA change rate. First, the positive critical phase jump is derived using the full-order model, as shown in Fig. 9(a). Then, the slope of the critical phase jump is calculated, as shown in Fig. 20. The peak in the slope corresponds to the maximal change rate of the BOA. κ_p at the peak slope is denoted by $\kappa_p^{\rm peak}$. The approximate design boundary is set as $\kappa_p^{\rm peak} + \Delta\kappa_p$, where $\Delta\kappa_p$ is 0.05 p.u. in this example. Table IV presents a comparison between the exact and approximate design boundaries. The approximate design boundary is close to the exact design boundary while simplifying the computation. This method provides a practical approach to identify the approximate design boundary and is a valuable tool for engineers and researchers.

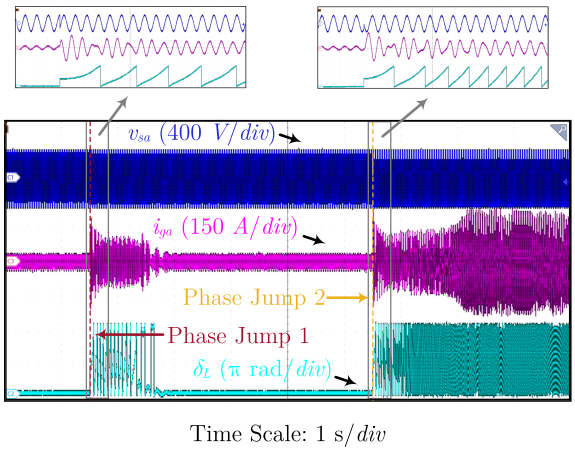

Fig. 21. Experimental waveforms of v_{sa}, i_{ga}, and δ_L after two subsequent phase jumps of -2.2 and -2.4 rad applied to v_s, with $\kappa_p = 0.4$ p.u. Other parameters adopt the default values.

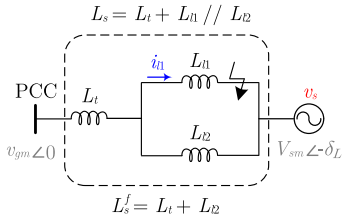

Fig. 22. Equivalent models of L_s and L_s^f.

VI. Experimental Verification

The *control hardware-in-loop* experiments have been performed to verify the analytical findings. The grid and the GFLC are emulated by the OPAL-RT equipment OP4512, while the control signals are generated using DSP TMS320F28377D. The default parameters in Table I are adopted unless otherwise stated, where the short-circuit ratio of the grid is 6.6. First, the phase jump disturbances are applied to v_s to validate the accuracy of the full-order model. As shown in Fig. 21, a phase jump of -2.2 rad cannot destabilize a GFLC with $\kappa_p = 0.4$ p.u. and other parameters adopting the default values. When the phase jump increases to -2.4 rad, the GFLC loses the synchronization, with δ_L diverging and i_{ga} soaring to a very high value. Despite the different stability results, the amplitude of i_{ga} is far from the reference value (30 A) during the transient process, which justifies the consideration of the nonideal current loop. These experimental results are consistent with the numerical result given in Fig. 9(a), where the full-order model predicts that the GFLC with $\kappa_p = 0.4$ p.u. has a critical phase jump of -2.3 rad.

Next, systems A ($\kappa_p = 0.202$ p.u., $f_c^{\rm cl} = 300$ Hz) and C ($\kappa_p = 0.312$ p.u., $f_c^{\rm cl} = 150$ Hz) described in Section V-A, which typify the GFLCs with very high and relatively low $f_c^{\rm cl}$, are tested with voltage dips and short-circuit faults to examine the proposed design principle. For clarity, the grid's equivalent inductance L_s is modeled as the series connection of a transformer inductance L_t and a double-circuit transmission line with $L_{l1} = L_{l2}$, as shown in Fig. 22. The grid's equivalent resistance r_s is processed in the same way. When a short-circuit fault occurs on L_{l1}, the relaying system disconnects the corresponding branch of the transmission line, leading to $L_s^f = L_t + L_{l2}$. Hence, a short-circuit fault with $L_s^f = 1.8$ p.u. means $L_t = 0.2$ p.u. and $L_{l1} = L_{l2} = 1.6$ p.u. With such modeling, the current of L_{l1} (i.e., i_{l1}) provides a clear indicator for the short-circuit fault.

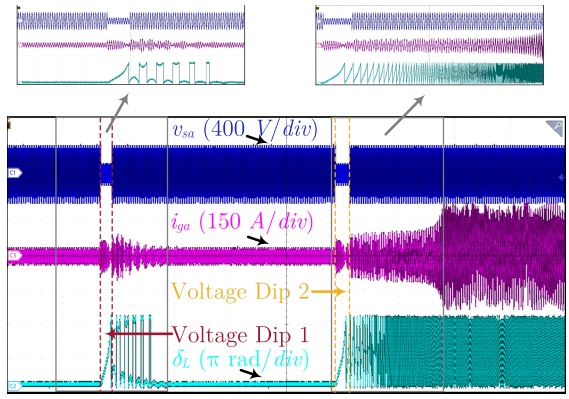

Fig. 23. Experimental waveforms of v_{sa}, i_{ga}, and δ_L after two subsequent voltage dips, with $V_{sm}^f = 0.35$ p.u., $\kappa_p = 0.202$ p.u., and $f_c^{\rm cl} = 300$ Hz. Other parameters adopt the default values. The first and second voltage dips last for 0.2 and 0.25 s, respectively.

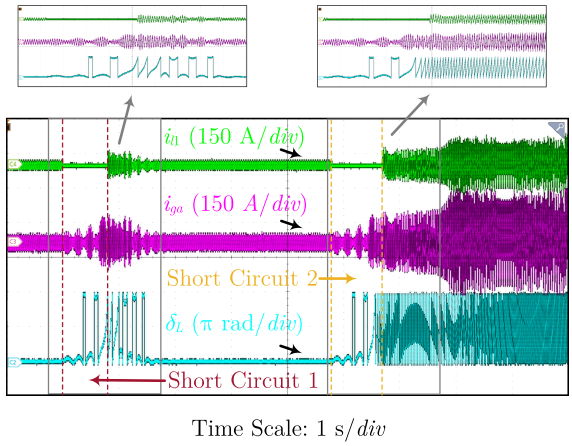

Fig. 24. Experimental waveforms of i_{l1}, i_{ga}, and δ_L after two subsequent short-circuit faults, with $L_s^f = 1.8$ p.u., $r_s^f = 1.8$ p.u., $\kappa_p = 0.312$ p.u., and $f_c^{\rm cl} = 150$ Hz. Other parameters adopt the default values. The first and second short-circuit faults last for 0.8 and 0.9 s, respectively.

Fig. 23 shows the response of system A under two subsequent voltage dips with $V_{sm}^f = 0.35$ p.u. While the fault depth is considerable, system A recovers the normal current and phase angle with the first voltage dip being cleared 0.2 s after its occurrence. Then, after the second voltage dip, which lasts for 0.25 s, system A falls into continuous oscillation. These experimental results are close to the numerical critical clearing time (0.30 s) given in Section V-A. Likewise, two short-circuits faults with $L_s^f = 1.8$ p.u. and $r_s^f = 1.8$ p.u. are applied to system C of Fig. 24. The first and second faults last for 0.8 and 0.9 s, respectively. The experimental results show that system C only diverges after the second short-circuit fault, which confirms the numerical critical clearing time given in Section V-A, i.e., 0.88 s.

The stability conclusions of the experiments are consistent with those of the numerical analysis. Hence, the experiments on systems A and C demonstrate the robust performance of the proposed design principle. Since the two systems have distinctive current loops, the experiments also corroborate the broad applicability of the proposed design principle to GFLCs with different current loop bandwidth.

VII. Conclusion

The nonideal current loop in the GFLC plays a decisive role in determining the dynamics of the system. Besides the adverse impact of current transients, this article also reveals the rapid contraction of the BOA as a result of the presence of the UPO near the SEP. For a relatively low current loop bandwidth (e.g., $f_c^{\mathrm{cl}} < 244.52$ Hz with the default setting), this UPO can be eliminated by triggering the saddle-node bifurcation of periodic orbits. For a very high current loop bandwidth (e.g., $f_c^{\mathrm{cl}} > 244.52$ Hz with the default setting), the same objective can be achieved by avoiding the center homoclinic bifurcation. Both cases can be implemented with the proposed numerical continuation or approximate method. With the proposed design principle, the BOA of the SEP becomes less sensitive to parameter changes, and consequently, a robust system can be easily designed.

References

[1] C. K. Tse, M. Huang, X. Zhang, D. Liu, and X. L. Li, "Circuits and systems issues in power electronics penetrated power grid," *IEEE Open J. Circuits Syst.*, vol. 1, pp. 140–156, Sep. 2020.

[2] Y. Li, Y. Gu, and T. C. Green, "Revisiting grid-forming and grid-following inverters: A duality theory," *IEEE Trans. Power Syst.*, vol. 37, no. 6, pp. 4541–4554, Nov. 2022.

[3] NERC Joint and WECC Staff Report, "900 MW fault induced solar photovoltaic resource interruption disturbance report," NERC, Atlanta, GA, USA, Tech. Rep., Feb. 2018. [Online]. Available: www.nerc.com

[4] NERC Joint and Texas RE Staff Report, "Odessa disturbance," NERC, Atlanta, GA, USA, Tech. Rep., Sep. 2021. [Online]. Available: www.nerc.com

[5] X. Wang, M. G. Taul, H. Wu, Y. Liao, F. Blaabjerg, and L. Harnefors, "Grid-synchronization stability of converter-based resources–An overview," *IEEE Open J. Ind. Appl.*, vol. 1, pp. 115–134, Aug. 2020.

[6] S.-K. Chung, "A phase tracking system for three phase utility interface inverters," *IEEE Trans. Power Electron.*, vol. 15, no. 3, pp. 431–438, May 2000.

[7] D. Dong, B. Wen, D. Boroyevich, P. Mattavelli, and Y. Xue, "Analysis of phase-locked loop low-frequency stability in three-phase grid-connected power converters considering impedance interactions," *IEEE Trans. Ind. Electron.*, vol. 62, no. 1, pp. 310–321, Jan. 2015.

[8] L. Harnefors, M. Bongiorno, and S. Lundberg, "Input-admittance calculation and shaping for controlled voltage-source converters," *IEEE Trans. Ind. Electron.*, vol. 54, no. 6, pp. 3323–3334, Dec. 2007.

[9] X. Li and H. Lin, "A design method of phase-locked loop for grid-connected converters considering the influence of current loops in weak grid," *IEEE J. Emerg. Sel. Topics Power Electron.*, vol. 8, no. 3, pp. 2420–2429, Sep. 2020.

[10] J. Zhao, M. Huang, and X. Zha, "Nonlinear analysis of PLL damping characteristics in weak-grid-tied inverters," *IEEE Trans. Circuits Syst. II*, vol. 67, no. 11, pp. 2752–2756, Nov. 2020.

[11] Q. Hu, L. Fu, F. Ma, and F. Ji, "Large signal synchronizing instability of PLL-based VSC connected to weak AC grid," *IEEE Trans. Power Syst.*, vol. 34, no. 4, pp. 3220–3229, Jul. 2019.

[12] X. Fu et al., "Large-signal stability of grid-forming and grid-following controls in voltage source converter: A comparative study," *IEEE Trans. Power Electron.*, vol. 36, no. 7, pp. 7832–7840, Jul. 2021.

[13] X. Li et al., "The largest estimated domain of attraction and its applications for transient stability analysis of PLL synchronization in weak-grid-connected VSCs," *IEEE Trans. Power Syst.*, early access, Jul. 06, 2022, doi: 10.1109/TPWRS.2022.3188887.

[14] H. Wu and X. Wang, "Design-oriented transient stability analysis of PLL-synchronized voltage-source converters," *IEEE Trans. Power Electron.*, vol. 35, no. 4, pp. 3573–3589, Apr. 2020.

[15] J. Zhao, M. Huang, H. Yan, C. K. Tse, and X. Zha, "Nonlinear and transient stability analysis of phase-locked loops in grid-connected converters," *IEEE Trans. Power Electron.*, vol. 36, no. 1, pp. 1018–1029, Jan. 2021.

[16] R. Ma, J. Li, J. Kurths, S. Cheng, and M. Zhan, "Generalized swing equation and transient synchronous stability with PLL-based VSC," *IEEE Trans. Energy Convers.*, vol. 37, no. 2, pp. 1428–1441, Jun. 2022.

[17] J. Chen, M. Liu, T. O'Donnell, and F. Milano, "Impact of current transients on the synchronization stability assessment of grid-feeding converters," *IEEE Trans. Power Syst.*, vol. 35, no. 5, pp. 4131–4134, Sep. 2020.

[18] Y. A. Kuznetsov, *Elements of Applied Bifurcation Theory*, 2nd ed., New York, NY, USA: Springer, 1998.

[19] Q. Hu, L. Fu, F. Ma, F. Ji, and Y. Zhang, "Analogized synchronous-generator model of PLL-based VSC and transient synchronizing stability of converter dominated power system," *IEEE Trans. Sustain. Energy*, vol. 12, no. 2, pp. 1174–1185, Apr. 2021.

[20] X. Fu, M. Huang, C. K. Tse, J. Yang, Y. Ling, and X. Zha, "Synchronization stability of grid-following VSC considering interactions of inner current loop and parallel-connected converters," *IEEE Trans. Smart Grid*, early access, Mar. 29, 2023, doi: 10.1109/TSG.2023.3262756.

[21] H.-D. Chiang, M. W. Hirsch, and F. F. Wu, "Stability regions of nonlinear autonomous dynamical systems," *IEEE Trans. Autom. Control*, vol. 33, no. 1, pp. 16–27, Jan. 1988.

[22] D. Moutevelis, J. Roldán-Pérez, M. Prodanovic, and S. Sanchez-Acevedo, "Bifurcation analysis of active electrical distribution networks considering load tap changers and power converter capacity limits," *IEEE Trans. Power Electron.*, vol. 37, no. 6, pp. 7230–7246, Jun. 2022.

[23] Y. Chen, R. Preece, and M. Barnes, "Identifying feasibility region boundaries in power systems with multiple VSCs," *IEEE Trans. Power Syst.*, vol. 38, no. 2, pp. 1229–1241, Mar. 2023.

[24] J. Yang, C. K. Tse, M. Huang, and X. Fu, "Homoclinic bifurcation of a grid-forming voltage source converter," *IEEE Trans. Power Electron.*, vol. 36, no. 11, pp. 13176–13187, Nov. 2021.

[25] X. Wang, X. Ruan, S. Liu, and C. K. Tse, "Full feedforward of grid voltage for grid-connected inverter with LCL filter to suppress current distortion due to grid voltage harmonics," *IEEE Trans. Power Electron.*, vol. 25, no. 12, pp. 3119–3127, Dec. 2010.

[26] D. Yang, X. Ruan, and H. Wu, "Impedance shaping of the grid-connected inverter with LCL filter to improve its adaptability to the weak grid condition," *IEEE Trans. Power Electron.*, vol. 29, no. 11, pp. 5795–5805, Nov. 2014.

[27] A. Dhooge, W. Govaerts, and Y. A. Kuznetsov, "MATCONT: A MATLAB package for numerical bifurcation analysis of ODEs," *ACM Trans. Math. Softw.*, vol. 29, no. 2, pp. 141–164, 2003.

Chao Charles Liu (Student Member, IEEE) received the B.S. and M.S. degrees from Wuhan University, Wuhan, China, in 2018 and 2021, respectively. He is currently working toward the Ph.D. degree with the Department of Electrical Engineering, City University of Hong Kong, Hong Kong, all in electrical engineering.

His research interests include transient stability of grid-connected converters, applications of nonlinear dynamics, and smart meter data analytics.

Jingxi Yang (Member, IEEE) received the B.S. and Ph.D. degrees in electrical engineering from Beijing Jiaotong University, Beijing, China, in 2014 and 2020, respectively.

He is currently a Postdoctoral Researcher with the Department of Electrical Engineering, City University of Hong Kong, Hong Kong. His research interests include nonlinear dynamics, bifurcation, and the stability of power-electronic-dominated power system.

Dr. Yang was the recipient of the the Outstanding Reviewer Award of the IEEE Transactions on Power Electronicsin 2021 and Excellent Reviewer Award of the Journal of Modern Power Systems and Clean Energy in 2022.

Chi K. Tse (Fellow, IEEE) received the B.Eng. (Hons.), with first-class honors, and the Ph.D. degrees in electrical engineering from the University of Melbourne, Parkville, VIC, Australia, in 1987 and 1991, respectively.

He is currently an Associate Vice President (Innovation) and Chair Professor of Electrical Engineering with the City University of Hong Kong, Hong Kong. His research interests include power electronics, nonlinear systems, and complex network applications.

Dr. Tse was the recipient of a number of research and invention prizes, including the IEEE CASS Charles A. Desoer Technical Achievement Award in 2022, and a few Best Paper Prizes from IEEE and other journals, as well as a Grand Prize and Gold Medal in Silicon Valley International Invention Festival 2019. He has been appointed to honorary professorship and distinguished fellowship by a few Australian, Canadian, and Chinese universities, including the Chang Jiang Scholar Chair Professor with the Huazhong University of Science and Technology, Honorary Professor of Melbourne University, and Distinguished Professor-at-Large with the University of Western Australia. He was a Panel Member of Hong Kong Research Grants Council, and Member of several professional and government committees. In 2005, 2010, and 2018, he was selected as an IEEE Distinguished Lecturer. In 2006, he chaired the IEEE CAS Technical Committee on Nonlinear Circuits and Systems. He is and was the Editor-in-Chief of IEEE TRANSACTIONS ON CIRCUITS AND SYSTEMS II (2016–2019), *IEEE Circuits and Systems Magazine* (2013–2016), and *IEICE Nonlinear Theory and Applications* (since 2013), an Associate Editor for a few other IEEE journals, and on the Editorial Board of IEEE PROCEEDINGS (2021–2022). He was on a number of IEEE committees, including the IEEE Fellows Committee and the IEEE Awards Committee, and chaired the Steering Committee for IEEE TRANSACTIONS ON NETWORK SCIENCE AND ENGINEERING.

Meng Huang (Member, IEEE) received the B.Eng. and M.Eng. degrees in electronic science and technology from the Huazhong University of Science and Technology, Wuhan, China, in 2006 and 2008, respectively, and the Ph.D. degree in electronic and information engineering from the Hong Kong Polytechnic University, Hong Kong, in 2013.

He is currently a Professor of the School of Electrical Engineering and Automation, Wuhan University, Wuhan. His research interests include safe operation and control of grid-connected systems.

Dr. Huang was the recipient of the Best Paper Award of the IEEE TRANSACTIONS ON POWER ELECTRONICSin 2016. He is an Editor of *International Journal of Circuit Theory and Applications*, and was the Guest Editor of IEEE JOURNAL OF EMERGING AND SELECTED TOPICS OF CIRCUITS AND SYSTEMS, and Guest Associate Editor for IEEE TRANSACTIONS ON INDUSTRIAL APPLICATIONS and IEEE JOURNAL OF EMERGING AND SELECTED TOPICS OF POWER ELECTRONICS.